A&A 669, A105 (2023)
https://doi.org/10.1051/0004-6361/202244400

Astronomy & Astrophysics

Using the slope of the brightness temperature continuum as a diagnostic tool for solar ALMA observations

Henrik Eklund[1,2,3], Mikołaj Szydlarski[1,2], and Sven Wedemeyer[1,2]

[1] Rosseland Centre for Solar Physics, University of Oslo, Postboks 1029, Blindern 0315 Oslo, Norway
[2] Institute of Theoretical Astrophysics, University of Oslo, Postboks 1029, Blindern 0315, Oslo, Norway
[3] Institute for Solar Physics, Department of Astronomy, Stockholm University AlbaNova University Centre, 106 91 Stockholm, Sweden
e-mail: henrik.eklund@astro.su.se

Received 1 July 2022 / Accepted 9 November 2022

ABSTRACT

Context. The intensity of radiation from the solar atmosphere at millimetre wavelengths is closely related to the plasma temperature, and the formation height of the radiation is wavelength dependent. It follows from this that the slope of the intensity continuum, or the brightness temperature continuum, samples the local gradient of the gas temperature of the sampled layers in the solar atmosphere.
Aims. We aim to show the added information and diagnostics potential of the solar atmosphere that comes with measuring the slope of the brightness temperature continuum.
Methods. We used solar observations from the Atacama Large Millimeter/sub-millimeter Array (ALMA) and estimated and predicted the slope using a numerical three-dimensional radiation-magnetohydrodynamic simulation. The slope was estimated by the differences between observables at wavelengths corresponding to different sub-bands at opposite sides of the ALMA receiver band 3 (2.8–3.2 mm) and band 6 (1.20–1.31 mm).
Results. The sign of the brightness temperature slope indicates temperature changes with increasing height at the sampled layers. A positive sign implies an increase in temperature, while a negative sign implies a temperature decrease. The differences in brightness temperature between the sub-bands across the field of view of the simulation typically span from −0.4 kK to 0.75 kK for band 3 and −0.2 kK to 0.3 kK at band 6. The network patches are dominated by large positive slopes, while the quiet-Sun region shows a mixture of positive and negative slopes. As the slope of the continuum is coupled to the small-scale dynamics, a negative slope is seen typically under quiet-Sun conditions as a result of propagating shock waves and the corresponding post-shock regions. The temporal evolution of the slopes can therefore be used to identify shocks. The observability of the slope of the brightness temperatures is estimated at bands 3 and 6 for different angular resolutions corresponding to ALMA observations. The simulations also show that the intensity of the radiation at bands 3 and 6 can simultaneously originate from several major components at different heights, which is strongly dependent on the small-scale dynamics and is seen in both quiet-Sun and network patches. Our in-depth analysis of selected shock waves that propagating upward in the atmosphere shows that the delay of shock signatures between two wavelengths (e.g., bands 6 and 3) does not necessarily reflect the propagation speed of the shock front, but might be cause by the rate of change in opacity of higher layers at these wavelengths.
Conclusions. The slope of the brightness temperature continuum sampled at different ALMA receiver sub-bands serves as an indicator of the slope of the local plasma temperature at the sampled heights in the atmosphere. This offers new diagnostic possibilities for measuring the underlying physical properties of small-scale dynamic features and thus contributes to the understanding of these features and the related transport of energy and heat in the chromosphere.

Key words. Sun: chromosphere – Sun: radio radiation – Sun: atmosphere – shock waves – techniques: interferometric – waves

1. Introduction

The continuum radiation at millimetre (mm) wavelengths originates from chromospheric heights and forms under local thermodynamic equilibrium conditions, so that the measured intensities are linked to the temperature of the emitting layers (see e.g., Wedemeyer et al. 2016, and references therein). With the start of regular solar observations with the Atacama Large Millimeter/sub-millimeter Array (ALMA) in 2016, the abilities of observing the Sun at mm wavelengths have taken a leap. Since then, much work has been done to develop and improve techniques for reconstructing high-cadence time-series from the interferometric measurement sets, which results in successfully produced science-ready data. Some of these high-level data sets are publicly available in the Solar ALMA Science Archive (SALSA; Henriques et al. 2022). An increasing number of studies making use of solar ALMA data has been published (see e.g., references within Henriques et al. 2022). In most of these works, the spectral domain is sacrificed, and the flux (and equivalently, the brightness temperatures) is reconstructed from combined interferometric data across the whole receiver band in order to increase the signal-to-noise ratio and thus the quality of the resulting images.

The intensities in each of the ALMA receiver bands are sampled in two pairs of sub-bands (Remijan et al. 2020). In the current work, we make use of these sub-bands by splitting the data, and we reconstruct images separately for each of the individual sub-bands. ALMA data split into sub-bands were analysed by Rodger et al. (2019) in order to estimate the optical thickness of radiation at band 3 (3.0 mm; Table 1) in observations of

X-ray bright points, and by Jafarzadeh et al. (2019), who compared brightness temperatures seen at the sub-bands of ALMA band 6 (1.25 mm) and simultaneous observations at ultraviolet wavelengths with the Interface Region Imaging Spectrograph (IRIS; De Pontieu et al. 2014) at and in the vicinity of a sunspot. Eklund et al. (2021a) investigated the diagnostic possibilities of sub-bands based on numerical simulations. The authors calculated the synthetic observables (using the advanced radiative transfer (ART) code de la Cruz Rodríguez et al. 2021) at different frequencies of ALMA receiver band 6 (1.20 mm–1.31 mm) from a 3D MHD Bifrost (Gudiksen et al. 2011) simulation of an enhanced network region with surrounding quiet Sun and analysed the slope of the brightness temperature continuum during the propagation of a shock wave. The authors showed that the slope of the brightness temperature continuum can be used to probe and study the small-scale features of the chromosphere.

In the current work, we further develop several aspects of ALMA sub-bands as a new diagnostic tool. We analyse the slope of the continuum brightness temperature of both bands 3 and 6 over the entire FOV of a *Bifrost* simulation (Carlsson et al. 2016), which shows different characteristics depending on the magnetic field topology, and extend the in-depth analysis of the propagating shock fronts in the quiet-Sun region. We also add a similar in-depth analysis of the network region. While the observability of small-scale dynamic brightening events at different angular resolutions and receiver bands of ALMA observations was investigated by Eklund et al. (2021b), in the current work, we also address the observability of the continuum slope at different angular resolutions corresponding to those of ALMA observations. In addition to the predictions based on numerical simulations, we also consider observational data of the quiet Sun, in which we detect shock-wave signatures, and we compare the slopes of the continuum brightness temperature to those from the simulations.

This work is structured in the following way. In Sect. 2 we describe the setup of the numerical simulations and methods of the radiative transfer calculations together with the degradation of the resulting observables for different angular resolutions. In Sect. 3, the results are presented, including the implications of the continuum slope as derived from the sub-band differences. In addition, the observability of the slope of the continuum at resolutions corresponding to ALMA observations is investigated. The subsequent comparison to observational solar ALMA data shows that the predictions from the simulations are confirmed by the observations. In Sect. 4 we discuss some topics that are important to keep in mind when observational data are analysed, and finally, in Sect. 5 we conclude.

2. Methods

2.1. Three-dimensional magnetohydrodynamic simulations

A three-dimensional 3D model of the solar atmosphere from the numerical radiative magnetohydrodynamic (MHD) code Bifrost was used (Gudiksen et al. 2011; Carlsson et al. 2016). The simulation accounts for non-equilibrium hydrogen ionisation. The simulation shows some network patches with opposite polarity of the magnetic field approximately 8 Mm apart, surrounded by quiet-Sun-like region. The simulation box has the extent $(x, y, z) = (24, 24, 17)$ Mm, with the bottom boundary at 2.5 Mm below the photosphere. In the vertical direction, (z), there are 496 cells with sizes varying between 19–100 km, with 20 km at the chromosphere. There are 504 cells in each of the horizontal directions (x, y) with a constant grid spacing of 48 km, resulting in a corresponding angular resolution of approximately 0.066 arcsec (at a distance of 1 AU). The boundary conditions in the horizontal directions are periodic. The simulation has the same setup as the publicly available version (Carlsson et al. 2016), but instead of the 10 s cadence, a higher-output cadence of 1 s was used. The duration of the simulation was approximately one hour. The publicly available version (at lower cadence) was for instance used to analyse the diagnostics at mm and submillimetre (submm) wavelengths by Loukitcheva et al. (2015, 2017) and to study the magnetic field topology by Jafarzadeh et al. (2017). The same high-cadence simulation that was used in the current work was previously used to study the diagnostic potential of solar ALMA observations by Wedemeyer et al. (2020), the impact of spatial resolution on ALMA observations of the Sun by Eklund et al. (2021b), and the variation in synthetic observables at mm wavelengths and the MHD properties of the atmosphere in connection to a propagating shock wave by Eklund et al. (2021a).

2.2. Brightness temperature maps at mm wavelengths corresponding to ALMA observations

In the current study, we analyse the observables at wavelengths corresponding to ALMA receiver band 3 (centred at 3.0 mm/100 GHz) and band 6 (centred at 1.3 mm/239 GHz). The observable continuum intensities at mm wavelengths were obtained by solving the equation for radiative transfer using the advanced radiative transfer (ART) code (de la Cruz Rodríguez et al. 2021) for each vertical column at each time step. The calculations were performed at three wavelengths in each spectral receiver sub-band at the respective minimum, medium, and maximum wavelengths, as indicated in Table 1. The intensities were then transformed into brightness temperatures using the Rayleigh-Jeans approximation (see e.g., Wilson et al. 2013). The resulting brightness temperature observables for each sub-band were then constructed by averaging the brightness temperatures at the three corresponding wavelengths.

We studied the slope of the brightness temperature continuum within the receiver bands, which we derived by the difference of brightness temperature between the outermost receiver sub-bands, SB4 and SB1, for each respective band (Table 1). The sub-band differences for bands 3 and 6 were calculated as

$$\Delta T_\mathrm{b}|_\mathrm{B3} = T_\mathrm{b}|_\mathrm{SB3.1} - T_\mathrm{b}|_\mathrm{SB3.4},$$
$$\Delta T_\mathrm{b}|_\mathrm{B6} = T_\mathrm{b}|_\mathrm{SB6.1} - T_\mathrm{b}|_\mathrm{SB6.4} \quad (1)$$

where $T_\mathrm{b}|_\mathrm{SB3.1}$, $T_\mathrm{b}|_\mathrm{SB3.4}$, $T_\mathrm{b}|_\mathrm{SB6.1}$, and $T_\mathrm{b}|_\mathrm{SB6.4}$ are the brightness temperatures for SB3.1, SB3.4, SB6.1, and SB6.4, respectively.

2.3. Synthesising mm maps with the angular resolution of ALMA observations

The physical locations of the 12 m antennas in the interferometric array can be reconfigured and arranged in different configurations. This changes the distribution of the distances and angles between the antennas. The vector between the antennas is referred to as a baseline. The distribution of the baselines determines at which scales and angles the interferometric array measures the target. Longer baselines sample smaller spatial scales in the source, and shorter baselines sample larger scales. The resulting angular resolutions of the antenna array configurations offered so far are of the same order or larger than the scales of typical small-scale dynamic events in the chromosphere, leaving

Table 1. Wavelengths and frequencies of the sub-bands of receiver bands 3 and 6 that were used for the radiative transfer calculations.

Sub-	Wavelength [mm]			Frequency [GHz]		
band	Min	Mid	Max	Min	Mid	Max
SB3.1	3.1893	3.2236	3.2586	92.0	93.0	94.0
SB3.2	3.1228	3.1557	3.1893	94.0	95.0	96.0
SB3.3	2.8282	2.8552	2.8826	104.0	105.0	106.0
SB3.4	2.7759	2.8018	2.8282	106.0	107.0	108.0
SB6.1	1.2978	1.3034	1.3091	229.0	230.0	231.0
SB6.2	1.2867	1.2922	1.2978	231.0	232.0	233.0
SB6.3	1.2137	1.2187	1.2236	245.0	246.0	247.0
SB6.4	1.2040	1.2088	1.2137	247.0	248.0	249.0

much of the small-scale dynamics unresolved (Eklund et al. 2020). The more extended antenna configurations are therefore more favourable for resolving chromospheric small-scale events (Eklund et al. 2021b).

We degraded the brightness temperature maps (Sect. 2.2) to the resolutions corresponding to interferometric ALMA observations. Synthesised beams with realistic sizes and shapes were acquired by performing synthetic interferometric ALMA observations, using the simobserve tool included in the Common Astronomy Software Applications package (CASA; v.6.1.0; McMullin et al. 2007), with different antenna array configurations and frequencies of the receiver sub-bands (Table 1). These beams were then used to degrade the brightness temperature maps by convolution. We refer to Eklund et al. (2021b, 2020) for more details. These authors used the same process. Because of the frequency dependence of the resolution, the receiver sub-bands have slightly different resolution. The resulting resolutions for each combination of array configurations C1–C7 and sub-bands 1 and 4 of receiver bands 3 and 6 are listed for reference in Table B.1.

2.4. Observational data

An observational data set taken with ALMA in band 3 (project ID: 2017.1.00653.S) in a quiet-Sun region close to the disc centre was used as comparison and validation of the results obtained in the simulations. The measurements were performed in the most commonly used antenna configuration for solar observations at band 3 (C3), resulting in a clean beam (main lobe of the point spread function; PSF) with an average size of $1.8'' \times 2.6''$ along the minor and major axis, respectively. The measurements were made on April 12, 2018, between 15:52 UT and 16:24 UT in four blocks of about 10 min each, separated by calibration gaps of about 2 min. The data were reduced with the Solar ALMA Pipeline (SoAP; Szydlarski et al. 2020 and in prep.) that largely automatises the process of phase self-calibration. The deconvolving process uses the CLEAN algorithm (Högbom 1974). The interferometric data were also combined with the total power measurements (White et al. 2017; Shimojo et al. 2017) to acquire absolute temperatures. We refer to Wedemeyer et al. (2020), Eklund et al. (2020) and Henriques et al. (2022) for summarised descriptions of the employed techniques of image reduction of the high-cadence time series. Images were constructed for each sub-band (Table 1) with an integration of 1 s. The same data set with images reconstructed from the full receiver band is available in the Solar ALMA Science Archive (SALSA; Henriques et al. 2022).

3. Results

3.1. Formation heights of radiation and corresponding plasma temperature

The formation heights of the radiation of the sub-bands of bands 3 and 6 are often determined as the heights at which the optical depth is unity for the corresponding wavelength, that is, $\tau_{3.2\,\mathrm{mm}} = 1.0$, $\tau_{2.8\,\mathrm{mm}} = 1.0$, $\tau_{1.3\,\mathrm{mm}} = 1.0$, and $\tau_{1.2\,\mathrm{mm}} = 1.0$. The resulting formation heights across the entire field-of-view of the simulation at the time of $t = 1600$ s in Fig. 1 show that the average formation height of the mm continuum is wavelength dependent, where the height of formation is larger for longer wavelength (see e.g., Vernazza et al. 1981; Loukitcheva et al. 2004; Wedemeyer-Böhm et al. 2007; Wilson et al. 2013; Wedemeyer et al. 2016). the statistics of the formation heights of the synthetic radiation at the ALMA receiver bands from the same Bifrost 3D model that was used here (Sect. 2.1) is presented by Eklund et al. (2021b). Their study considered the average values over the whole receiver bands. They confirmed that the formation height increases with wavelength on average, and that it is larger at the network patches than at the surrounding quiet Sun on average.

The corresponding differences in formation height of the sub-bands of bands 3 and 6 (SB3.1-SB3.4 and SB6.1-SB6.4) are given in Fig. 1c and f, respectively. The difference in formation height (i.e. $z(\tau = 1.0)_\lambda$ at the respective wavelength) between the sub-bands is positive at all times, with SB3.1 forming higher up than SB3.4 and SB6.1 forming higher up than SB6.4. This is the case at all times and locations throughout the entire simulation box (see Sect. 2.1). We point out that this trend is also seen at all times for each of the ALMA receiver bands between band 3 (100 GHz) – band 10 (867 GHz; see Eklund et al. 2021b, for details). Data for these bands were also calculated, but for simplicity, we did not include all bands in the detailed analysis here. The consistent order of formation height of the sub-bands comes from the wavelength dependence of the opacity. We thus have for the formation height z

$$z(\tau_{\mathrm{SB1}} = 1.0) > z(\tau_{\mathrm{SB4}} = 1.0), \tag{2}$$

where the radiation of SB1 has a longer wavelength than that of SB4 for each band (Table 1).

An optical depth of $\tau(\nu) = 1.0$ can serve as a good first approximation of the formation height of the radiation, for instance in the case of 1D atmospheric models, such as the static VAL model (Vernazza et al. 1981) and also with the introduction of plane-parallel propagating shocks (see e.g., Loukitcheva et al. 2004; Carlsson & Stein 2002, and references therein). However, in a 3D environment with more complex dynamics due to propagating and interfering waves, the contribution to the intensity of the ALMA bands can come from several major components at different heights along the line of sight. Examples are shown in Fig. 2, where the contribution functions of SB3.1, SB3.4, SB6.1, and SB6.4 are shown for a slit across the FOV at $y = -15$ arcsec.

The change in opacity from one sub-band to another is not very large, and the major components of the contribution functions of the two sub-bands originate largely from the same heights at a given location, which is the case for both receiver bands 3 and 6 (Fig. 2). These heights, displayed in (Figs. 2c and f), are therefore probed by the sub-bands, and the brightness temperature differences (slope of the brightness temperature continuum) provides information on the slope of the local plasma temperature for these heights. For simplicity, we therefore focus on the contribution function of a single sub-band in

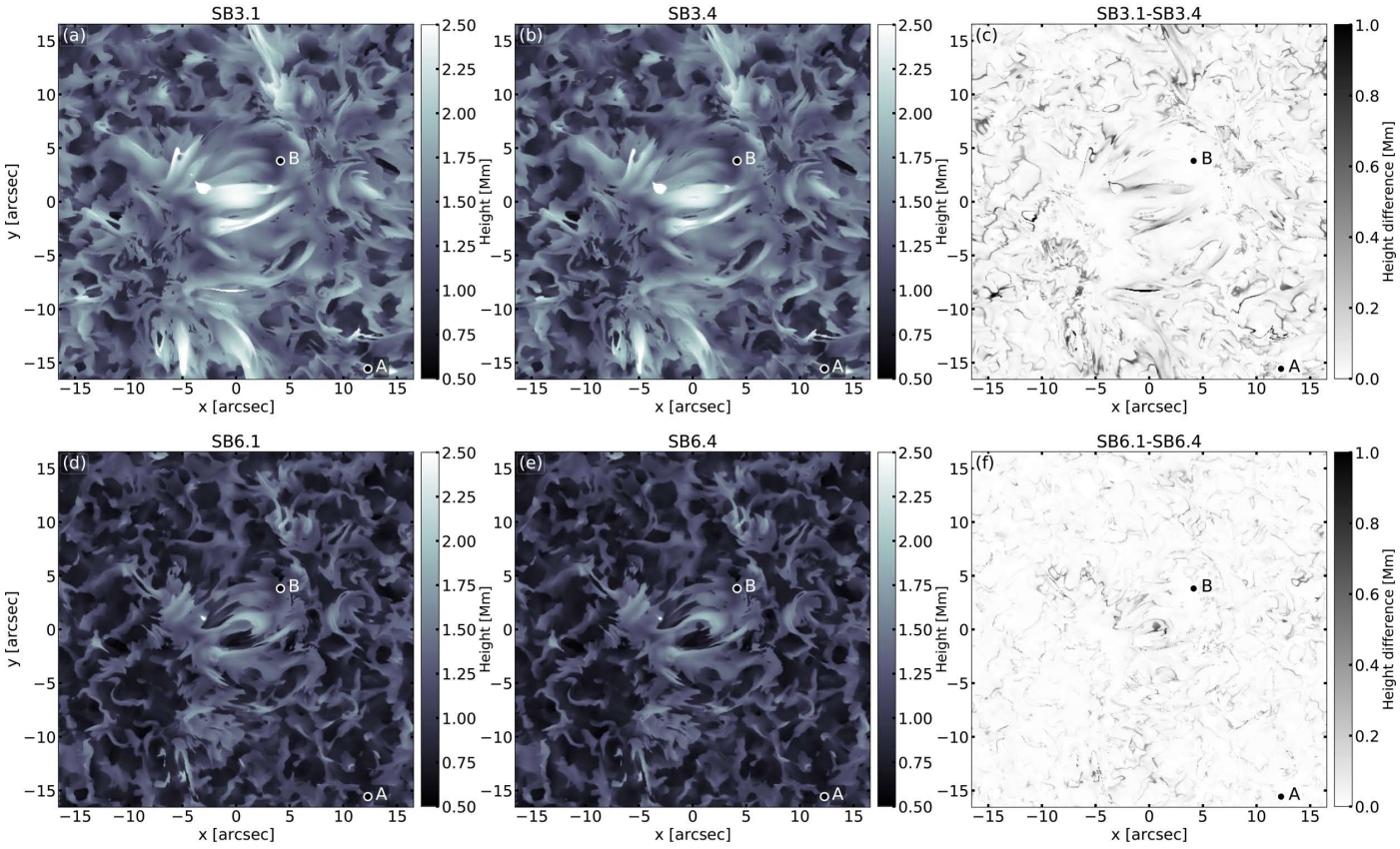

Fig. 1. Formation hieght of the radiation at (a) SB3.1 ($\tau_{3.2\,\mathrm{mm}} = 1.0$), (b) SB3.4 ($\tau_{2.8\,\mathrm{mm}} = 1.0$), (c) difference in height between SB3.1 and SB3.4, (d) SB6.1 ($\tau_{1.3\,\mathrm{mm}} = 1.0$), (e) SB6.4 ($\tau_{1.2\,\mathrm{mm}} = 1.0$) and (f) difference in height between SB3.1 and SB3.4. The selected locations A and B for the time-series analysis (Figs. 3–5) are marked for reference. The colour scale of the sub-band differences (c) and (f) are positive at all times (they are not absolute) and are capped to 1.0 Mm from 1.42 Mm at band 3 (c) and 1.17 Mm at band 6 (f) in order to reveal the small-scale structures.

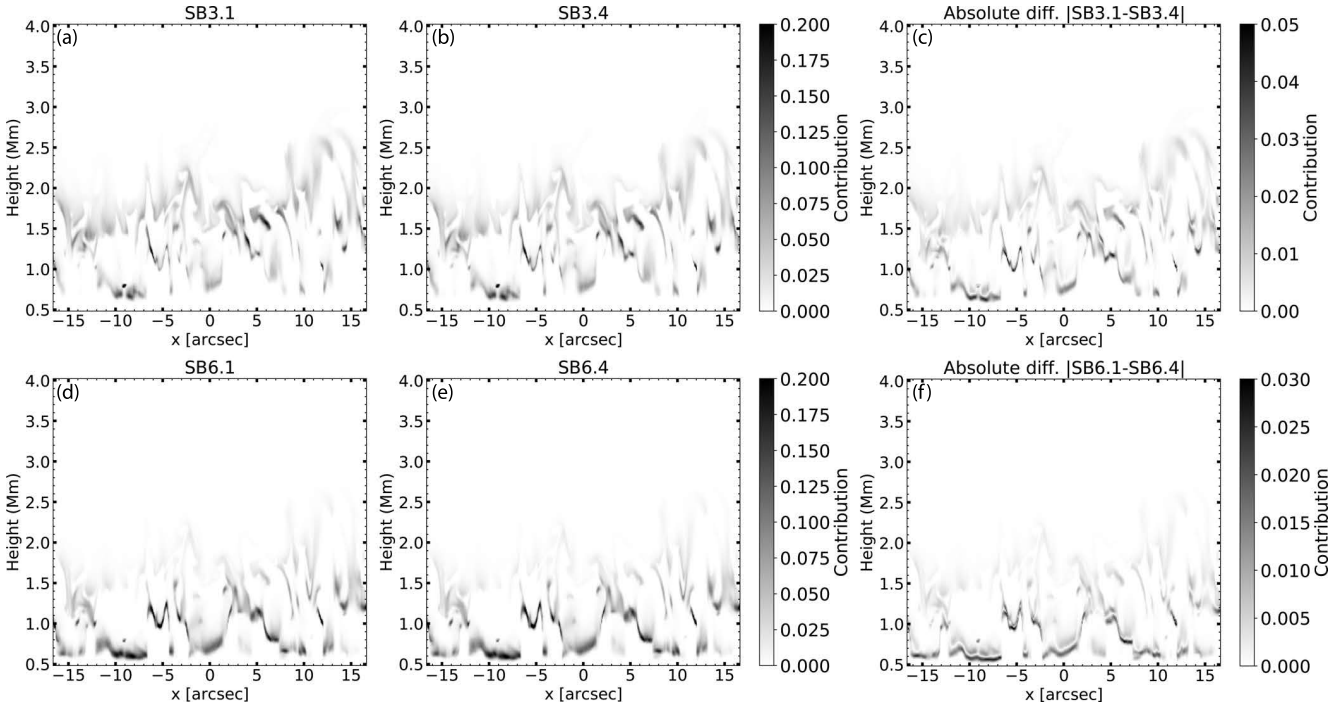

Fig. 2. Contribution to the total brightness temperature as function of height along a slit at $y = -15$ arcsec of SB3.1 (a), SB3.4 (b), the absolute difference between the SB3.1-SB3.4 (c), SB6.1 (d), SB6.4 (e) and the absolute difference between the SB6.1-SB6.4 (f). The colour scales are different at the different bands.

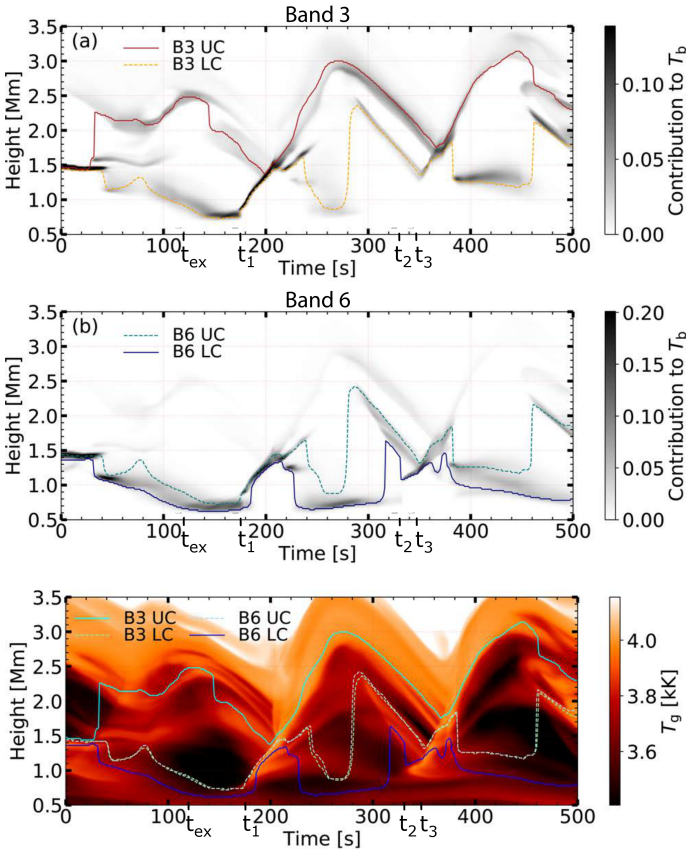

Fig. 3. Time evolution of contribution functions and plasma temperature for a column in the quiet Sun at location A (Fig. 1), with the shock-wave event studied in detail in Eklund et al. (2021a). The contribution function of band 3 (a) and band 6 (b) with heights of 0.25 and 0.80 times the contribution function integrated from the top is marked by the dashed and solid lines, respectively. (c) Plasma temperature with each of the representative heights of the two components of bands 3 and 6 marked for reference. The ticks t_{ex} and $t_1 - t_3$ mark the times for the in-depth discussion in connection to Figs. 4 and 7.

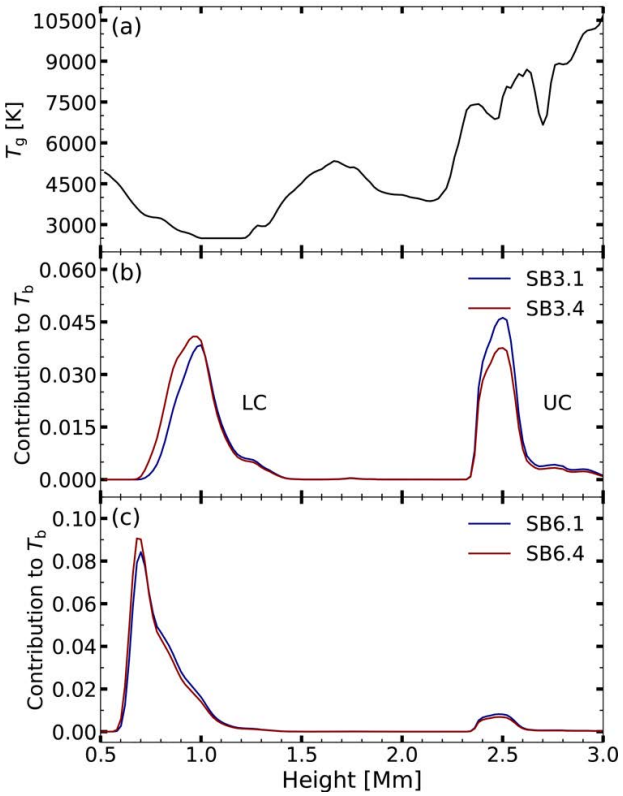

Fig. 4. Plasma temperature and contribution functions plotted against height in the atmosphere for one time step, t_{ex} = 120 s, of the shock wave (see, Fig. 3) at location A (Fig. 1). (a) Plasma temperature as function of height. (b) Contribution functions of SB3.1 and SB3.4, each showing a lower and an upper component, marked LC and UC, respectively. (c) Contribution functions of SB6.1 and SB6.4.

each receiver band in the following in-depth analysis. The components of the contributions to the intensities of bands 3 and 6 show large and overlapping height ranges (Fig. 2). Band 3 more often shows a strong component at high altitudes simultaneously with a component at lower altitudes, while band 6 shows a more concentrated contribution to the lower component and only a weak upper component.

In Fig. 3 we show the evolution of the contribution functions of SB3.1, SB3.4, SB6.1, and SB6.4 for a time series (t = 0–500 s) of propagating shock waves in quiet-Sun conditions (see Eklund et al. 2021b, for the identification of the regions in the simulaiton), in the corner of the simulation box at $(x, y) = (-15.6, 12.3)$ arcsec (location A in Fig. 1). The beginning of the time-series (t = 0–300 s) was presented in detail by Eklund et al. (2021a), including the excitation of a shock wave around t = 175 s. Here we show an additional 200 s of the time series at the same location, which includes the excitation of an additional shock around t = 350 s. The shock shows a magnitude of the brightening excess that is commonly seen for events in the simulation under quiet-Sun conditions (Eklund et al. 2021b). In the time series at this location, band 3 shows two main components in the contribution to the brightness temperatures at most times (Fig. 3a). We refer to the two components as the upper component (UC) and the lower component (LC). The heights of the two components are at most times well estimated by 0.25 (UC) and 0.80 (LC) of the integrated contribution function from the top (marked by dashed and solid lines in Fig. 3). There are some exceptions where the contribution is fairly concentrated in a single component, which is when the upwardly propagating shock front intersects with the down-falling gas at t = 200 s and t = 370 s. The vertical velocities of the time series are shown in Appendix A for reference. At these times, the UC and LC of band 3 merge and sample the same height range, and, as we show below (Sect. 3.2.2), the brightness temperature is high at these points.

While band 3 displays significant contribution from both the LC and the UC at significantly different heights at most times (Fig. 3a), band 6 shows a mix between occasions with weaker contributions from the upper layers, leaving both the LC and UC sampling the concentrated contribution function at similar heights (i.e. t = 120 s in Fig. 3b) and with stronger contributions from the upper layers, giving rise to a significant difference in height between the LC and UC (i.e. t = 300 s). The relative contribution between the LC and the UC is complex and dependent on the wavelength of the radiation and the small-scale dynamic structures in the atmosphere. In quiet-Sun conditions, the propagating shocks give rise to the conditions where there is a UC of the contribution to the brightness temperatures (up to ~3.0–3.5 Mm at band 3 and up to ~2.5–3.0 Mm at band 6 of the selected example in Fig. 3). The UC is seen both when the mm wavelength radiation tracks the propagating shock upwards and in the corresponding post-shock regions. However, the shocks

do not give rise to a dense enough upper layer to be optically thick in neither band 3 nor band 6. A lower layer is therefore simultaneously sampled, hence the presence of the LC. The cool low-density post-shock regions can separate the LC from the UC by several Mm. See Eklund et al. (2021a) for further details on the atmospheric perturbation by the shock.

The shock starting around $t = 178$ s is sampled by both band 3 (LC) and band 6 simultaneously at a height $z \approx 0.7$ Mm (Fig. 3) and is tracked up to around 1.4 Mm at $t = 210$ s. Thereafter, the UC of band 6 and LC of band 3 tracks a secondary component of the shock (hook-shaped feature in Fig. 3), see also Eklund et al. (2021a) up to about 1.7 Mm at $t = 240$ s, and the UC of band 3 tracks the shock front all way up to about 3.0 Mm.

As an illustrative example, the contribution to the intensities as function of height for bands 3 and 6 at $t = 120$ s of the time series is displayed together with the plasma temperature as a function of height in Fig. 4 on the same x-axis to facilitate reading out the slope of the plasma temperature at the sampled heights. Here, the contribution functions of SB6.1 and SB6.4 each show one main component, centred around 0.7 Mm, and only a very small contribution at heights around 2.5 Mm. At heights around 0.7 Mm sampled by band 6, the plasma temperature decreases with increasing height (Fig. 4a). The contribution functions of SB3.1 and SB3.4 at $t = 120$ s, on the other hand, each show two main components, the LC around 1.0 Mm, and the UC around 2.5 Mm. Around the heights of the LC, the plasma temperature decreases slightly with increasing height, and around the heights of the UC, the plasma temperature increases (on average over the UC) with height (Fig. 4a). The slope of the gas temperature at the sampled layers is reflected by the brightness temperature difference between the sub-bands, which we discuss further in Sect. 3.2.2.

Similar to the example of shocks under quiet-Sun conditions (Fig. 3), a time series of the contribution functions and the corresponding plasma temperature at a location in the network region (location B in Fig. 1) is given in Fig. 5. During the first 200 s, both bands 3 and 6 show contribution functions with one well-concentrated main component at a similar height. Band 6, however, shows two main components to the contribution function towards the end of the time series. The formation heights at location B in the network region are less dynamic than at location A in the quiet Sun. The corresponding vertical velocities for the time series are given in Appendix A.

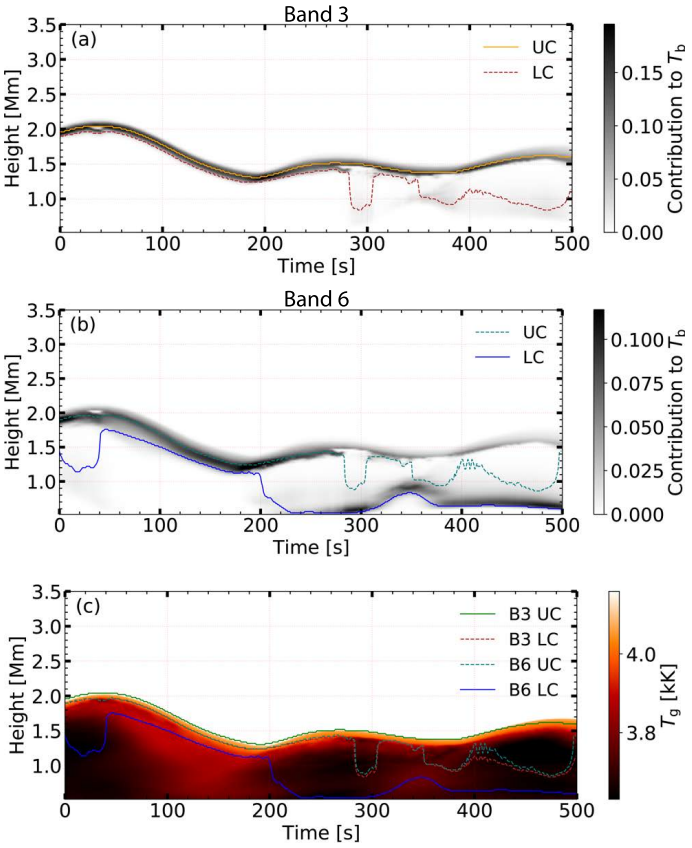

Fig. 5. Time evolution of contribution functions and plasma temperature for a column in the network patches at $(x, y) = (3.8, 4.2)$ arcsec, marked as location B in the FOV maps (Fig. 1). Top panel: contribution function of band 3 with heights of 0.25 and 0.8 times the contribution function integrated from the top marked by the dashed and solid lines, respectively. Middle panel: same as the top panel for band 6. Bottom panel: plasma temperature with representative formation heights of bands 3 and 6 marked with dashed and solid lines, respectively. The formation height at $\tau = 1.0$ of both sub-bands is indicated in the respective row to facilitate comparison.

3.2. Synthetic observables, and difference in brightness temperature between sub-bands

3.2.1. Variation over the field of view

The synthetic observables of the sub-bands of bands 3 and 6 at $t = 1600$ s are presented in Fig. 6. The brightness temperatures ranges agree with those for the corresponding full-band maps, which were analysed in detail for different areas in the field of view by Eklund et al. (2021b). For band 3, the average brightness temperatures over the entire FOV are 7710 K at SB3.1 and only 7430 K at SB3.4, with values of up to 21 050 K at a few locations in the central network patches. These values (see Eklund et al. 2021b, for the corresponding full-band temperature distributions) agree well with average values reported for observational full-band 3 ALMA data of the quiet Sun, such as 7056 K for internetwork (IN) and 7694 K for network (NW) regions by Alissandrakis et al. (2020) and 7228 K (IN) and 7588 K (NW) by Wedemeyer et al. (2020). They also agree with observations with other instruments, such as the Nobeyama 45 m telescope, measuring 7700 ± 310 K at 2.6 mm (close to SB3.4; Table 1) averaged over the whole solar disc (Iwai et al. 2017). Band 6 shows significantly lower average temperatures of 6190 K at SB6.1 and 6090 K at SB6.4, and maximum temperatures of only up to 13 310 K.

The difference in the brightness temperatures between SB3.1 and SB3.4, $\Delta T_b|_{B3}$ (see Eq. (1)), across the FOV of Fig. 6c shows values between −377 K and −2320 K. There are distinct differences in the magnitude and the sign of T_b sub-band differences with different magnetic field topology. This effect is expected as the magnetic field interferes with propagating shock fronts, resulting in reflection or transformation into other magneto-acoustic wave modes. Canopies of magnetic fibrils can obscure the view of the shocks at lower heights. As a result, shock-front signatures at mm wavelengths are not seen as frequently in areas with a greater magnetic field strength (Eklund et al. 2020), such as the magnetic field footpoints in the central FOV (Fig. 6).

The largest $\Delta T_b|_{B3}$ are seen at the few locations displaying the highest temperatures in the central network patches. In the surrounding region of network patches, a substantially positive $\Delta T_b|_{B3}$ of several hundreds K is displayed in most locations. Occasionally occurrences with negative sub-band T_b difference are recorded as well, most notable in band 3, in the area

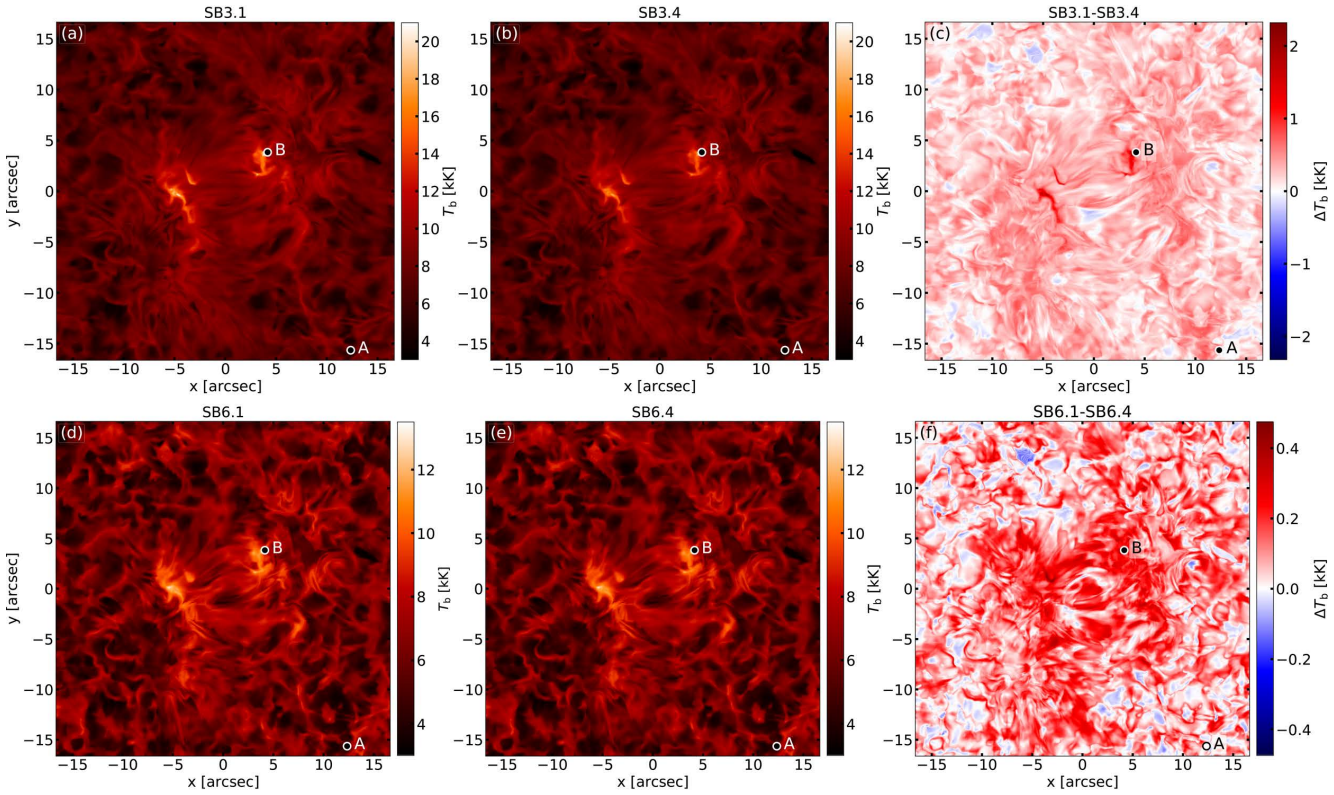

Fig. 6. Brightness temperatures of sub-bands of bands 3 and 6. (a) $T_b|_{SB3.1}$, (b) $T_b|_{SB3.4}$, (c) $\Delta T_b|_{B3}$ ($T_b|_{SB3.1} - T_b|_{SB3.4}$), (d) $T_b|_{SB6.1}$, (e) $T_b|_{SB6.4}$, and (f) $\Delta T_b|_{B6}$ ($T_b|_{SB6.1} - T_b|_{SB6.4}$). The selected locations A and B for the time-series analysis are marked for reference. The colour scales of the two receiver bands are different.

between the magnetic field footpoints where the magnetic loops are mostly horizontally inclined at the heights of ALMA bands 3 and 6 (Jafarzadeh et al. 2017; see also Fig. 1). Most of the occasions with low or even negative $\Delta T_b|_{B3}$ values are seen in the corners of the FOV, which are representative of quiet-Sun conditions. The sub-band differences in band 6, $\Delta T_b|_{B6}$, show a similar picture, but with lower magnitudes, with values only between −182 K and 474 K.

Because the order of the formation height of the sub-bands consistently remains the same (Sect. 3.1), the slope of the continuum brightness temperature consequently reflects the slope of plasma temperature at the sampled heights. A positive ΔT_b indicates a plasma temperature that increases with height at the sampled layer. A positive value therefore agrees with the classical models of the chromosphere, in which the stratification of the average temperature increases with height (see e.g., Vernazza et al. 1981). A negative ΔT_b indicates a decreasing plasma temperature with increasing height at the sampled layer.

In the network patches in the central parts of the FOV (Fig. 6c), which show high $\Delta T_b|_{B3}$ values, the differences in formation height of the sub-bands ($z(\tau_{SB3.1} = 1.0) - z(\tau_{SB3.4} = 1.0)$) are low (Fig. 1c), indicating a steep gradient of the local plasma temperature increasing with height at the sampled layers of band 3. In quiet-Sun conditions in the outskirts of the FOV of the synthetic maps, positive and negative ΔT_b values are mixed at bands 3 and 6. The gradient of the brightness temperature continuum and therefore also the occurrence of negative continuum slopes are coupled to the dynamics in the atmosphere, and the negative continuum slopes mostly occur at locations towards the corners of the FOV (Fig. 6), showing quiet-Sun conditions in which the dynamics is largely affected by shock propagation. The negative continuum slopes at band 3 ($\Delta T_b|_{B3}$) is stronger than in band 6 ($\Delta T_b|_{B6}$), but band 6 shows more occurrences and more small-scale structures of the negative continuum slopes than band 3.

3.2.2. Time series of brightness temperatures at selected locations

Quiet Sun with propagating shock waves at location A. The temporal evolution of the brightness temperatures of the sub-bands of bands 3 and 6 at the location of propagating shock waves in the quiet Sun (location A in Fig. 6) is shown in Fig 7a between t = 0–500 s. Propagating shock fronts give rise to an increase in temperature and therefore brightness temperature at mm wavelengths (Carlsson & Stein 1992; Loukitcheva et al. 2004, 2006; Eklund et al. 2021a; Wedemeyer-Böhm et al. 2007). The beginning of the brightness temperature increase of the first shock front occurs almost simultaneously for both bands 3 and 6 around t_1 = 178 s, while there is a delay from sampling the second shock front at t_2 = 332 s (around z = 1.1 Mm) at band 6 to t_3 = 345 s (around z = 1.27 Mm) at band 3. This accounts for a vertical shock propagation speed of about 13.1 kms^{-1}, which agrees well with the speed of the first shock around t_1 = 178 s (Eklund et al. 2021a). The delay between the sub-bands is small, however, ∼1–2 s at both bands, leaving the signatures barely resolved by the vertical grid spacing of the simulation (Sect. 2.1). Both bands 3 and 6 largely sample at low heights (∼0.7 Mm) right before they start to probe the first shock around t_1 = 178 s (Fig. 3). Consequently, there is no delay of the signatures in the observables between the bands (Fig. 7). However, before the second shock front (e.g., around t = 300 s), band 3 only

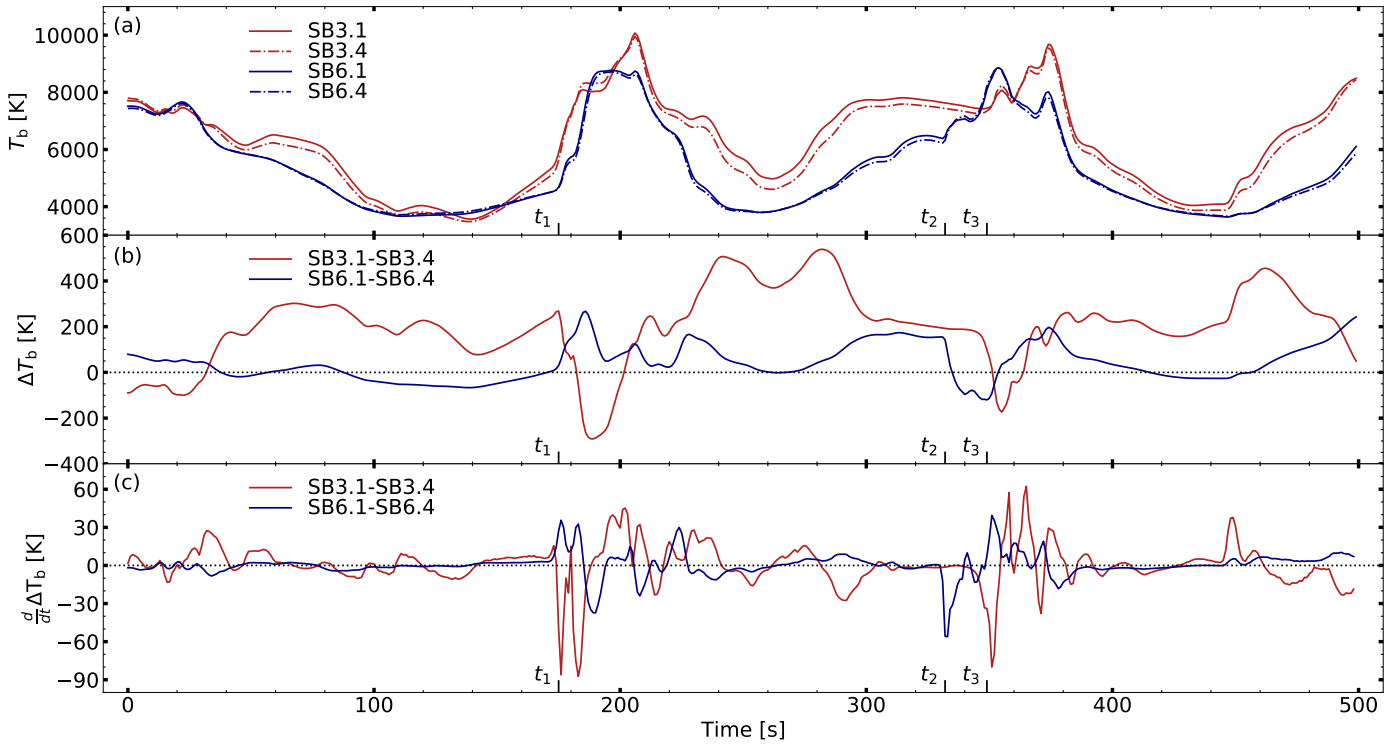

Fig. 7. Evolution of brightness temperatures and sub-band differences at the location of the propagating shock wave (location A) between $t = 0$–500 s. (a) Brightness temperatures of SB3.1, SB3.4, SB6.1, and SB6.4. (b) Brightness temperature differences between the sub-bands $\Delta T_b|_{B3}$ ($T_b|_{SB3.1} - T_b|_{SB3.4}$) and $\Delta T_b|_{B6}$ ($T_b|_{SB6.1} - T_b|_{SB6.4}$). (c) Time-derivative of the sub-band differences $\Delta T_b|_{B3}$ and $\Delta T_b|_{B6}$. In each panel, the time at which the different bands start to sample the shock waves is marked with tick marks t_1 (bands 3 and 6), t_2 (band 6), and t_3 (band 3).

samples the down-falling plasma, while band 6 samples both the down-falling plasma and also partly plasma at low heights around 0.7 Mm and therefore captures the shock front about 13 s earlier than band 3. This delay of 13 s does not directly reflect the propagation speed of the shock front, but it instead gives an indication on the difference in opacity of the upper component measuring the down-falling plasma between bands 3 and 6.

The slope of the continuum is sensitive to sudden changes in the local atmosphere. Propagating shock waves therefore show themselves in the time-evolution of the sub-band differences (Fig. 7b). The brightness temperature differences between the sub-bands illustrated in Fig. 7b reflect the slope of the plasma temperatures at the heights sampled by each receiver band, shown in Fig. 3c. At band 3, there is a sub-band difference of SB3.1 − SB3.4, with negative $\Delta T_b|_{B3}$ values down to −291 K, between approximately $t = 180$–200 s, while the first shock front is probed. Band 6, on the other hand, shows an increase in sub-band difference. Prior to the first shock front at $t_1 = 178$ s, band 6 probes the plasma around 0.7 Mm (Fig. 3), showing a negative sub-band difference down to about −70 K (Fig. 7b), indicating a decreasing temperature with increasing height at the sampled layers, which is seen to be the case in Fig. 3 and in Fig. 4 of the specific example at $t_{ex} = 120$ s. Band 3 probes the down-falling plasma prior to the shock front at $t_1 = 178$ s from about 2.5 Mm to 1.5 Mm and shows a large positive sub-band difference around 150–200 K. This indicates a temperature that increases with height at the sampled layers, which also is confirmed in Figs. 3 and 4. At the time of $t = 120$ s, ($\Delta T_b|_{B6}$) shows a negative value and ($\Delta T_b|_{B3}$) a positive value, which agrees with what we expected from the specific example in Fig. 4. The propagating shock front at $t_1 = 178$ s then gives rise to a rapid increase in sub-band difference at band 6 and a rapid decrease at band 3. The fact that both of the receiver bands 3 and 6 probe the down-falling hot plasma at high altitudes prior to the second shock front (Fig. 3) is indicated by the large positive sub-band differences (around $t = 320$ s in Fig. 7b). The second propagating shock front therefore gives rise to negative continuum slopes in both bands, similarly as for band 3 in the case of the first shock front. The shock signatures in the slope of the continuum thus differs depending on the physical conditions of the local atmosphere that the shock faces and if the receiver band probes plasma at low altitudes or down-falling plasma at higher altitudes prior to and after the sampling of the propagating shock front. The time-derivatives of the sub-band differences (Fig. 7c) can in addition be used to reveal the shock fronts, and in particular, to more precisely see when the shock fronts start to be probed. For instance, at $t_1 = 178$ s, the peak at band 6 and the peak towards negative values at band 3, are prominent. Similarly, the start of probing the second shock front at $t_2 = 332$ s in band 6 and $t_3 = 345$ s at band 3 is indicated by the the steep peaks towards negative values.

Some occasions, however, show an increase in brightness temperature that is not produced by a shock front. Around $t = 275$ s, there is a quite rapid increase in T_b at band 3, which, as the contribution function and plasma temperature in Fig. 3 show, is not due to sampling of a upwards-propagating shock front, but rather by probing the down-falling plasma. The sub-band difference shows no indication of shocks, however, and is steadily large between 400 and 500 K. Between $t = 270$ s and $t = 310$ s, there is a steady increase in brightness temperature at band 6 at the same time as a slow increase of the sub-band difference is seen, which originates in a gradual shift from the lower component in the contribution at heights around 0.7 Mm to the upper component sampling the down-falling plasma. This is difficult to

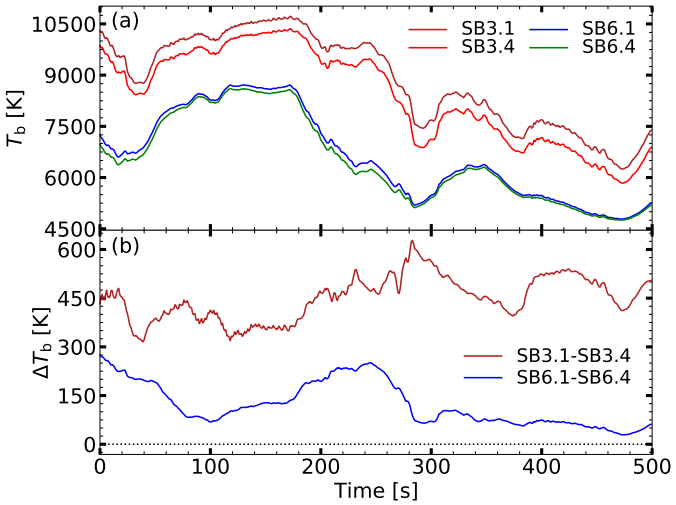

Fig. 8. Evolution of brightness temperatures and sub-band differences at location B in the network region between t = 0–500 s. (a) Brightness temperatures of SB3.1, SB3.4, SB6.1, and SB6.4. (b) Sub-band differences $\Delta T_b|_{B3}$ ($T_b|_{SB3.1} - T_b|_{SB3.4}$) and $\Delta T_b|_{B6}$ ($T_b|_{SB6.1} - T_b|_{SB6.4}$).

interpret by considering the T_b alone, but the evolution of $\Delta T_b|_{B6}$ reveals the change from probing a layer with a fainter to a steeper gradient of the plasma temperature increasing with height. The difference between the sub-bands thus gives slightly more information, which can for instance be used to distinguish the shock fronts from possible other phenomena or changes in opacity at different layers, leading to changes in formation height of the radiation at the sampled wavelengths.

Network region at location B. The brightness temperatures are higher on average in the network region than in the quiet Sun. We refer to Eklund et al. (2021b), for example, for statistics on the brightness temperatures at different regions in the Bifrost model at the different ALMA receiver bands. In Fig. 8 we show the time evolution of the resulting brightness temperatures at location B in the network region (Fig. 6). This time series thus corresponds to the contribution functions shown in Fig. 5. Here, the brightness temperatures are significantly higher at band 3 than at band 6, by an average value of 2050 K over the time series. There are variations in brightness temperature over time also of some thousands of degrees with similar characteristics at both bands. The differences in brightness temperature between the sub-bands are constantly positive at both bands 3 and 6, which agrees with what is seen at most locations in the central network region in the ΔT_b maps (Fig. 6c and f). The positive sub-band differences reflect the increasing temperature with height at the sampled layers, which is indicated in Fig. 5, and the larger ΔT_b at band 3 than at band 6 shows the steeper gradient of the plasma temperature at the layer sampled by band 3 at higher altitude than the layer sampled by band 6. The variations in ΔT_b are more prominent at band 3 than at band 6 (Fig. 5b), but are partly coupled to the variations in the brightness temperatures (Fig. 5a) at both bands.

3.3. Sub-band differences with degraded angular resolution

The T_b differences between SB1 and SB4 for bands 3 and 6 over the entire FOV of a snapshot (t = 1600 s) are presented in Fig. 9 at the original resolution and at the resolutions corresponding to ALMA observations with array configurations C1–C7. Array configuration C1 is the most compact, resulting in an angular resolution down to about 3.4 arcsec and 1.5 arcsec at band 3 and band 6, respectively. The more extended configuration C7, which is not yet available for solar observing, would result in a resolution down to about 0.23 arcsec and 10.10 arcsec at band 3 and band 6, respectively. The analysis here extends to higher resolution than for the array configurations commissioned for solar observations (C4 at band 3 and C3 at band 6). The corresponding angular resolution for each array configuration and receiver sub-band are listed for reference in Table B.1.

The variations in T_b differences between the sub-bands are driven by the chromospheric small-scale dynamics (Sect. 3.2). The typical spatial scales of the small-scale dynamics are of the same order or smaller than the resolution offered for solar ALMA observations (see e.g., Eklund et al. 2021b, and references therein). The observability of the spatial fine structure of the sub-band differences therefore very strongly depends on the chosen resolution of the observations. Consequently, the small-scale structure in the maps of the sub-band difference becomes less pronounced at degraded resolution. As a result, negative continuum slopes occur less often or not at all in the degraded maps (Fig. 9). The negative sub-band differences is completely non-apparent in band 3 at the angular resolutions corresponding to array configuration C1 and C2 (c.f., Table B.1). This clearly shows that the positive values of sub-band differences are the dominating feature. A minimum resolution corresponding to array configuration C3 is necessary for the negative sub-band difference to be apparent in band 3. With a better angular resolution corresponding to the wider array configuration C4, which is available for band 3 at the time of writing, more of the structures of the negative sub-band differences are apparent, but a resolution corresponding to C5 or higher should be preferred to show the stronger correlation to the structures seen in the map at the original resolution. At band 6, the negative sub-band differences ($\Delta T_b|_{B6}$) are apparent at all offered resolutions (for solar observations), also corresponding to the most compact array configuration C1 (Fig. 9). This is a result of the significantly higher angular resolution at the wavelengths around ∼1.25 mm of band 6 compared to around ∼3.0 mm at band 3 (Table 1), which preserves the observability of the features with the strongest negative sub-band difference. However, the ($\Delta T_b|_{B6}$) structures at sub-arcsec scales are only apparent at resolutions corresponding to array configuration C3 or higher, although for the magnitudes of sub-band differences of structures at sub-arcsec to be well sampled, the resolution of C3 is not satisfying. At locations in which the sub-band difference is uniform over a large area in comparison to the clean beam, such as in the areas containing the magnetic footpoints in the centre of the FOV (dark red patches in Fig. 9), the magnitude and the large-scale structures of the sub-band differences also remain discernible at the degraded resolution.

The time series of the sub-band differences of bands 3 and 6 at location A (Fig. 6) during the passage of the shock waves in the maps with different angular resolutions are given in Fig. 10. During the first shock wave around t = 180 s, for example, the negative sub-band difference at band 3 of −291 K at the original resolution (Fig. 10a) appears only as −73 K at the resolution of the solar ALMA observations in this work (Sect. 3.4; array configuration C3). Similarly, the high positive $\Delta T_b|_{B3}$ values of up to 550 K between t = 230 s and t = 290 s are shown only as a couple hundred K at the resolution of C3. Already at the resolution of C4 at band 3 (Table B.1), the magnitudes of the sub-band differences are much more accurately sampled. The magnitudes of the sub-band differences at band 6 are lower than at band 3, which might cause weaker features to be missed at the degraded

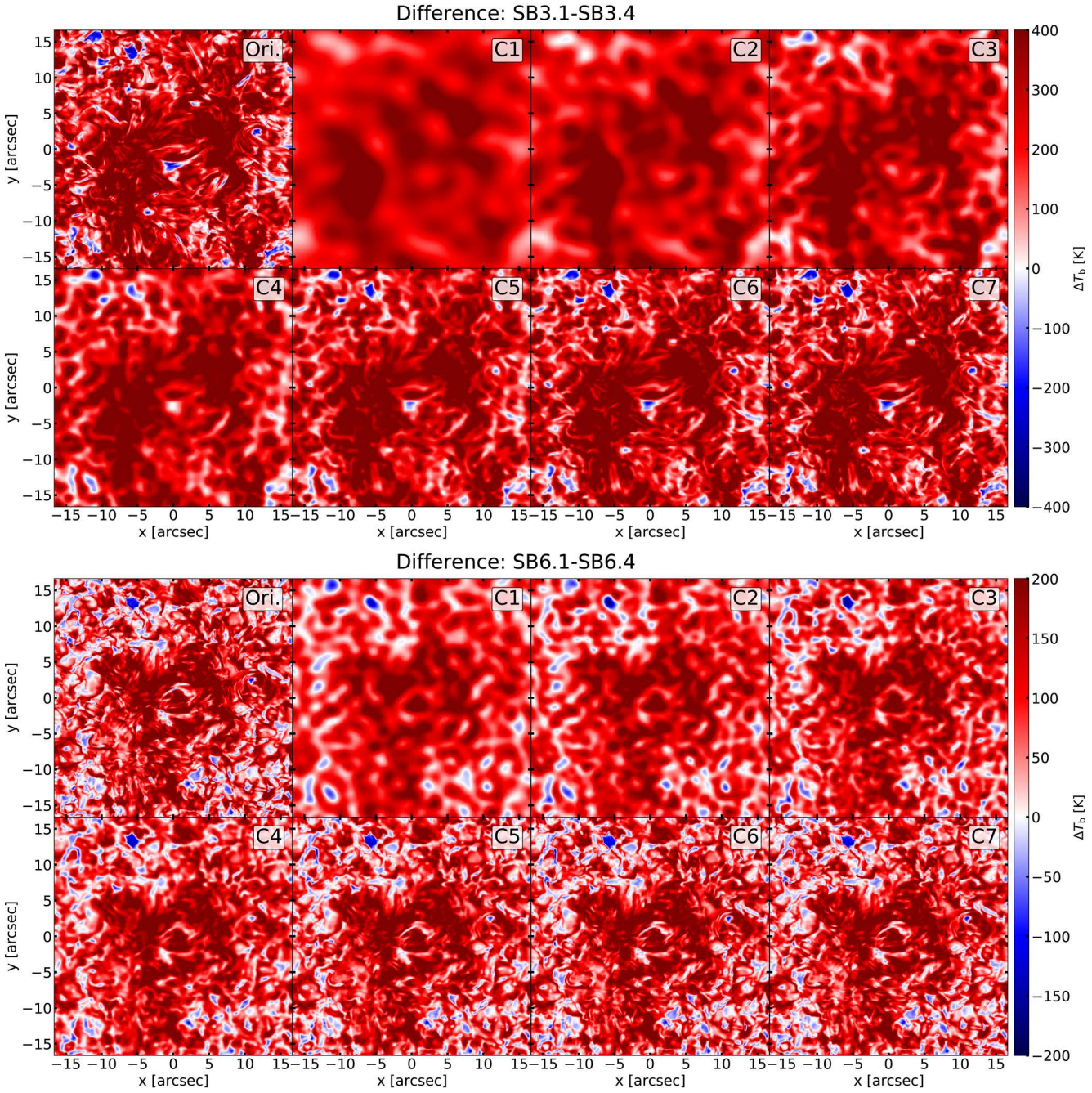

Fig. 9. Sub-band brightness temperature difference at band 3, $\Delta T_b|_{B3}$, (top panels) and at band 6, $\Delta T_b|_{B6}$, (bottom panels) at the original resolution of the numerical model and at the resolutions corresponding to array configurations C1 to C7 for the respective receiver sub-band (Table B.1). The T_b maps are individually degraded to the respective resolution before the differences were calculated.

resolutions. For instance, a resolution corresponding to at least array configuration C5 is required to sample the negative sub-band difference at band 6 between $t = 90$ s and $t = 170$ s. It is thus expected that only a negative continuum slope is visible at the angular resolution of the observations with ALMA as conducted so far at some locations where the ΔT_b is significantly large and the structure giving rise to negative continuum slopes is large or at least at the same order of size as the resolution element of the observations.

However, the general features in the temporal evolution of the sub-band differences and the shock-wave signatures are still preserved at the degraded resolutions, which correspond to the higher resolutions currently offered for solar observations (i.e. minimum C3 at both bands). Therefore, an analysis of the sub-band differences in the observations provides much complementary information to the information obtained in the analysis of the full-band images.

3.4. Observational data

The brightness temperature of a snapshot of observational quiet-Sun data at SB3.1 (Table 1) is shown in Fig. 11a for a FOV of approximately 50 × 50 arcsec. This image was made by adding the total power measurement to the interferometric data. Using only the interferometric data at each sub-band, we obtain the sub-band difference, $\Delta T_b|_{B3} = T_b|_{SB3.1} - T_b|_{SB3.4}$ that corresponds

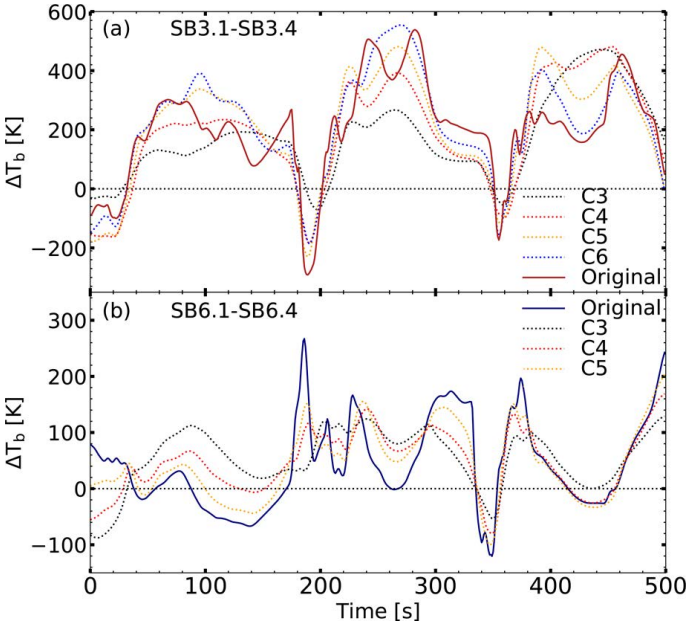

Fig. 10. Time evolution of the sub-band T_b differences of the time series at location A at the different angular resolutions. (a) T_b difference between sub-bands 3.1 and 3.4 at the original resolution (solid red line) and at the degraded resolutions corresponding to array configurations C3, C4, C5, and C6 (coloured dotted lines). (b) T_b difference between sub-bands 6.1 and 6.4 at the original resolution (solid blue line) and at the degraded resolutions corresponding to array configurations C3, C4, and C5 (coloured dotted lines). The horizontal dotted black lines show the level of $\Delta T_b = 0$.

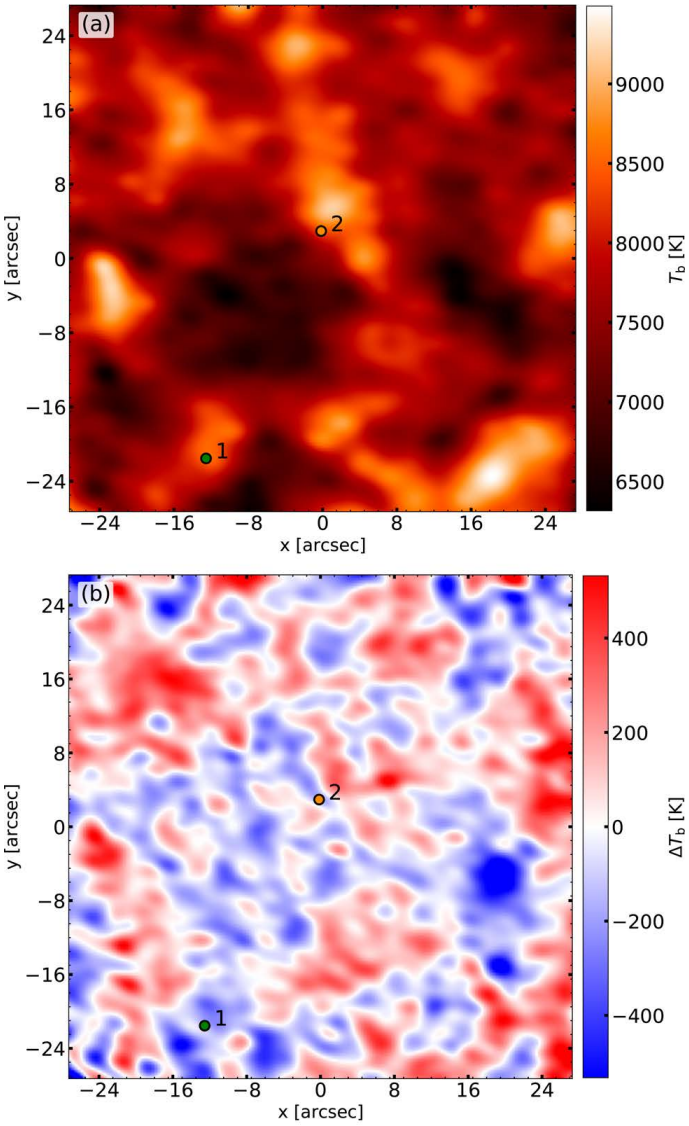

Fig. 11. Brightness temperature and sub-band brightness temperature difference of the FOV of the observational band 3 data at $t = 290$ s. (a) Brightness temperature of SB3.1 as constructed by adding the total power data to the interferometric data. (b) Difference of the brightness temperature between the sub-bands, $\Delta T_b|_{B3} = T_b|_{SB3.1} - T_b|_{SB3.4}$ derived from the interferometric data at each sub-band. The span of $\Delta T_b|_{B3}$ is between −1150 K and 670 K, but the colour scale was limited to −500 K to 500 K to reveal the small-scale structures. The locations of the two selected brightening events are marked by the green and orange markers.

to the same snapshot (Fig. 11b). The colour scale was capped at −500 K to 500 K from the span of approximately −1150 K to 670 K. The sub-band differences are strongly coupled to the small-scale features. The observational data feature quiet Sun without any network patches (Jafarzadeh et al. 2021), which in the simulation is only comparable to the corners of the FOV (Fig. 9). The features with negative sub-band difference in the observation (Fig. 11b) show typical scales up to about 5 arcsec, which agrees well with the scales of the few features that are seen in the corners of the simulation (Fig. 9; note the different extents of the FOVs). A detailed study of the magnetic field strength and topology would need to be made for a global comparison of the sub-band differences of the observational data and the simulation. For now, we resort to analysing several small-scale brightening events in the observational data. The temporal evolution of the two events is shown in Fig. 12. These events, event 1 and event 2, show an excess brightness temperature of approximately 450 K and 400 K at SB3.1, respectively, measured as the difference between the base temperature at the temporal local minimum and the peak temperature (see Eklund et al. 2020 for the definition and selection criteria of the base temperature). The temporal signatures and magnitudes of the brightening events agree with what is expected for shocks propagating upward largely vertically through the chromosphere (Eklund et al. 2021a), at the angular resolution of the observations (Eklund et al. 2021b). The differences between the sub-bands ($\Delta T_b|_{B3}$) for the two events are given in Figs. 12b and e, where boxcar averages over 10 s, removing potential high-frequency noise, are also shown. $\Delta T_b|_{B3}$ spans between approximately −200 and 200 K during event 1 and between −240 and 100 K during event 2. The temporal evolution of the $\Delta T_b|_{B3}$ of both event 1 and event 2 is consistent with what is seen for the synthetic observables of the shock-wave event in the simulation (Fig. 7b) at band 3. The sub-band difference at $t = 225$ s decreases rapidly for event 1 and at $t = 220$ s for event 2, simultaneously with the start of the increase in brightness temperature (indicated by t_1 and t_3 in Fig. 7 for the events in the simulation), which is visible in the graph of the time-derivative of the sub-band differences in Figs. 12c and f. The $\Delta T_b|_{B3}$ shows negative values during the increase in brightness temperature (Figs. 12a and d). At the end of the T_b peak, $\Delta T_b|_{B3}$ increase abruptly, reflected by peaks in the time derivatives (Figs. 12c and f).

The degradation of the excess temperatures that is due to the angular resolution might be further corrected for in an in-depth analysis of the brightening events (Eklund 2022). However, in

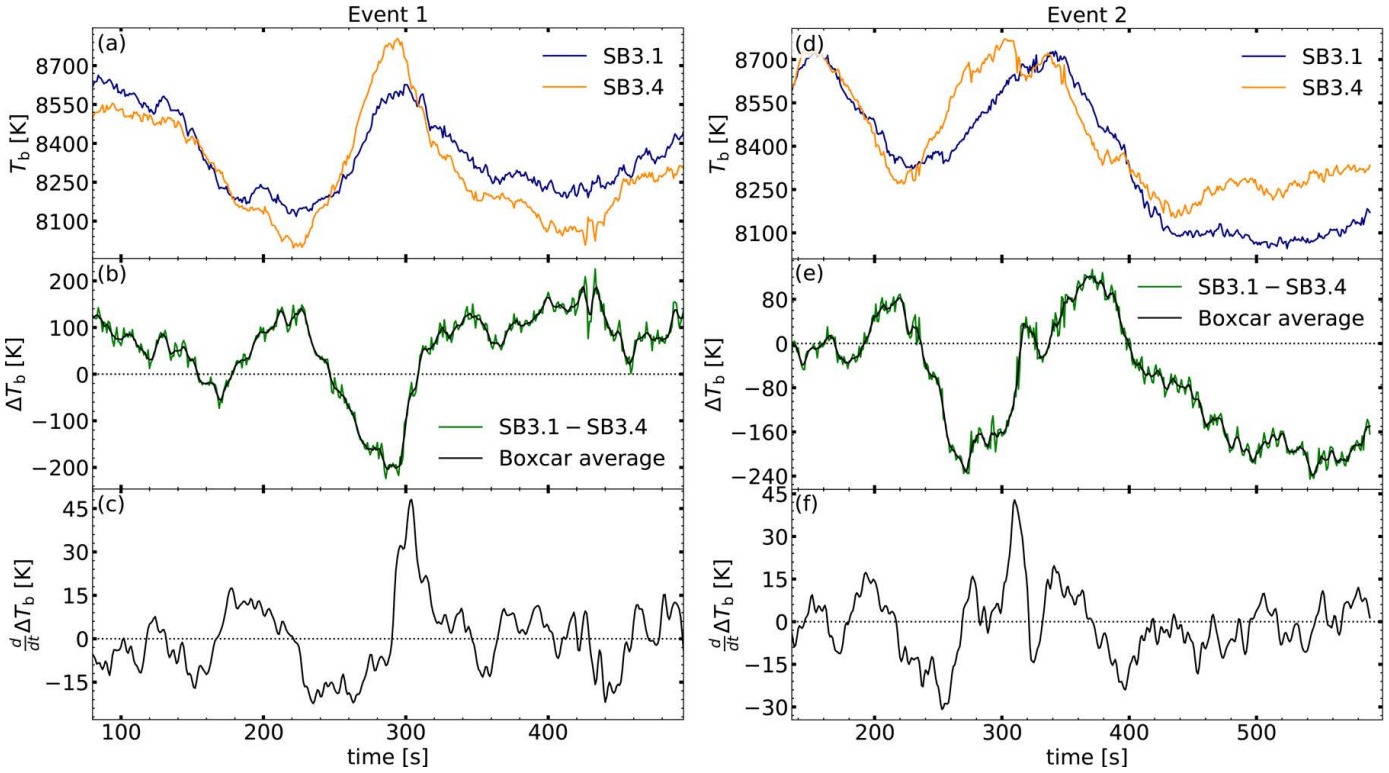

Fig. 12. Temporal evolution of the brightness temperatures at of the two selected brightenings in the observational data. Left column: Event 1. Right column: Event 2. The locations of the events are indicated in the FOV of Fig. 11. (a,d) Brightness temperatures of SB3.1 and SB3.4. (b,e) Brightness temperature differences between the sub-bands $\Delta T_{b|B3}$. The green graph shows the original data, and the black curve schows a boxcar average over 10 s. (c,f) Time derivative of the (boxcar-averaged) sub-band differences.

the current work, it is evident that the sub-band differences are large enough to be detected in the ALMA data, and they can be used to identify shock signatures.

4. Discussion

4.1. Techniques for image reconstruction

The synthetic brightness temperature maps based on the simulations are assumed to be equivalent to optimal observations with a sampling on all scales and orientations (i.e. full Fourier sampling), enabling the study of sub-band differences and their connection to the atmospheric structures. We analysed the combined brightness temperatures over each of the outermost sub-bands, that is, SB1 and SB4 of bands 3 and 6 (Table 1). A reconstruction of the images over a larger span of frequencies, for instance pairwise over both the neighbouring sub-bands SB1 and SB2, and comparison of this with the image of both SB3 and SB4 might improve the signal-to-noise ratio. This would also diminish the magnitude of the sub-band differences, however, and would therefore limit this as a tool of measuring the slope of the continuum. The time integration used in the observations was one second, which might be extended to a few more seconds in order to enlarge the signal-to-noise ratio. However, this might leave rapid small-scale dynamic features unresolved. The optimised integration over frequency and time to boost the signal-to-noise ratio while preserving the important features thus depends on the specific science case and is worth exploring further.

As the sub-band differences are coupled to the small-scale dynamics, successful observations with more extended array configurations with a resulting higher angular resolution would provide a very useful tool for probing the dynamic structures of the solar atmosphere. However, it still needs to be determined to which degree it is feasible to perform solar measurements at more extended array configurations.

The detected signatures in the observational data agree well with what is seen in the simulation, and this study of the sub-band differences serves as a proof of concept of the usage of sub-band differences for the analysis of solar ALMA observations. Nonetheless, further commissioning on calibrating the spectral domain of the ALMA receiver bands and deriving uncertainties on the sub-band differences is required.

4.2. Evaluation of the sub-band differences

The sub-band brightness temperature difference (Eq. (1)) is dependent on the thermal structure of the atmosphere and on the separation in the formation height of the sub-bands. Of the currently offered ALMA bands, band 3 shows the largest wavelength difference between the outermost sub-bands, SB1 and SB4 (Fig. 1), which results in a larger difference on average in formation height of the sub-bands compared to the higher-numbered receiver bands (Table 1). However, even though the sub-band differences become more evident at longer wavelengths, the observational angular resolution decreases with increasing wavelength, which counteracts the ability to measure the sub-band differences. The typical scales of dynamic features such as the brightening events presented in Eklund et al. (2021b) are of the order of or even lower than the angular resolutions currently offered for solar ALMA observations, which limits the observability of these features. Consequently, the small-scale structures of the sub-band differences are more prominent at the highest resolution offered for solar ALMA observations of band 6 than those of band 3 (Fig. 9).

The sub-band differences could be made larger if only the intensities from the spectral channels in outermost part of the sub-bands, with maximum wavelength seperation, were combined in the imaging process. This would result in a lower signal-to-noise ratio, however.

4.3. Atmospheric modelling and resulting radiation formation heights

The resulting wavelength dependence of the formation height of the radiation depends on the physical processes included in the modelling of the atmosphere and on the radiative transfer calculations. Martínez-Sykora et al. (2020) included the treatment of ion-neutral interactions (ambipolar diffusion) in their 2.5-dimensional Bifrost simulations and reported a similar formation height of the synthetic observables at wavelengths of ALMA band 3 and band 6 in active region and network conditions. They also reported that when they accounted for the non-equilibrium ionisation rate of hydrogen and helium, the contribution functions were more concentrated to narrower height ranges for both ALMA bands, although there are occasions with two significantly strong components of the contribution function at different heights. However, in the current work, bands 3 and 6 also show a similar formation height to a certain extent at location B in the magnetic network region (Fig. 5), in particular when the contribution function is concentrated and constrained to a rather narrow layer (up to $\sim t = 200$ s), where after band 6, two main components are visible.

The brightness temperatures of the ALMA data are also useful for creating atmospheric models through inversion (da Silva Santos et al. 2018). It can be difficult to create models with a good fit of the ALMA brightness temperatures to a specific layer in the atmosphere (Hofmann et al. 2022), however, which can be explained by contributions from several main components at different heights (as shown in Figs. 3–5).

5. Conclusion

The slope of the brightness temperature continuum provides information on the gradient of the plasma temperature of the local atmosphere at the sampled layers. A negative (positive) continuum slope indicates a decreasing (increasing) temperature with increasing height. The time-dependent variations in the continuum slope reveal the evolution of the gradient of the plasma temperature at the sampled layers and can provide indications of the vertical structure of the atmosphere. Propagating shocks give rise to large variations of the continuum slope, which can therefore be used to identify and distinguish shock waves from other events.

The simulations showed that multiple main components at different heights often contribute to the measured brightness temperatures in both bands 3 and 6, in particular in the quiet-Sun region with propagating shocks, but also in the network region. As a consequence, the delay of signatures of upwardly propagating shock waves between two sub-bands or different receiver bands is not necessarily a measurement of the propagation speed of the shock front. It can rather be a measurement of the difference in opacity of the upper component between the two sub-bands or receiver bands. When both bands sample a relaxed post-shock region that is perturbed by a new shock wave, there is no significant delay in the signature of the shock wave between bands 3 and 6. Under quiet-Sun conditions, band 3 more often shows multiple components at different heights than band 6. This consequently makes the interpretation of the measured brightness temperatures in the quiet Sun more complex at band 3 than at band 6. In the network region, band 6 more often shows a second main (lower) component than band 3. In certain locations in the network region of the simulation, both bands 3 and 6 display one single component of the contribution function at similar heights. However, the sub-band differences can give an indication whether more than one main component contributes to the measured brightness temperature and their relative height of formation. It can therefore be very valuable to include the sub-band differences in the analysis of solar ALMA data.

The observability and usage of the sub-band differences are limited by the angular resolution, because the scales of many dynamic features are of the same order of scales as the angular resolutions currently offered for solar ALMA observations. While much of the small-scale structures remains unresolved, many features show a large sub-band difference that is apparent also at the angular resolution currently offered for solar observations. Resulting from the high angular resolution, band 6 can therefore be used as a meaningful diagnostics tool for detecting and using the sub-band differences. Even though the numerical simulations indicate that occurrences of large sub-band differences frequently occur at band 3 as well, the lower angular resolution of the observations at band 3 limits their observability, and negative continuum slopes are observable at locations showing a very strong negative sub-band difference or over a well-extended area of negative sub-band difference (large in comparison to the resolution element).

The results from the simulations were compared to observational data of a quiet-Sun region, where the evolution of several shock-wave signatures was shown in detail. The variances in sub-band differences and the negative continuum slopes that are seen in connection to the shock signatures agree with what is seen in the simulations when the limited spatial resolution of the observations is taken into account. The sub-band differences can thus be used as a method for detecting or differentiating shock-wave signatures from other eventual transient events in the observational data.

With the aid of the sub-band differences, further work can be developed, in particular towards coupling the dynamical structures to the temperature stratification of the atmosphere at the sampled layers and identifying the dynamical structures that give rise to several main components of the contribution function. In conclusion, the slope of the brightness temperature continuum can be used as a diagnostics tool in the analysis of solar ALMA data and give invaluable information that contributes to the understanding of the dynamics that takes place and to the transport of energy in the solar atmosphere.

Acknowledgements. This work was supported by the SolarALMA project, which has received funding from the European Research Council (ERC) under the European Union's Horizon 2020 research and innovation programme (grant agreement No. 682462), and by the Research Council of Norway through its Centres of Excellence scheme, project number 262622, and through grants of computing time from the Programme for Supercomputing. HE was supported through the CHROMATIC project (2016.0019) funded by the Knut and Alice Wallenberg foundation. This paper makes use of the following ALMA data: ADS/JAO.ALMA#2017.1.00653.S. ALMA is a partnership of ESO (representing its member states), NSF (USA) and NINS (Japan), together with NRC(Canada), MOST and ASIAA (Taiwan), and KASI (Republic of Korea), in co-operation with the Republic of Chile. The Joint ALMA Observatory is operated by ESO, AUI/NRAO and NAOJ. We are grateful to the many colleagues who contributed to developing the solar observing modes for ALMA and for support from the ALMA Regional Centres.

References

Alissandrakis, C. E., Nindos, A., Bastian, T. S., & Patsourakos, S. 2020, A&A, 640, A57
Carlsson, M., & Stein, R. F. 1992, ApJ, 397, L59
Carlsson, M., & Stein, R. F. 2002, ApJ, 572, 626
Carlsson, M., Hansteen, V. H., Gudiksen, B. V., Leenaarts, J., & De Pontieu, B. 2016, A&A, 585, A4
da Silva Santos, J. M., de la Cruz Rodríguez, J., & Leenaarts, J. 2018, A&A, 620, A124
de la Cruz Rodríguez, J., Szydlarski, M., & Wedemeyer, S. 2021, ART: Advanced (and fast) Radiative Transfer code for Solar Physics, https://github.com/SolarAlma/ART
De Pontieu, B., Title, A. M., Lemen, J. R., et al. 2014, Sol. Phys., 289, 2733
Eklund, H. 2022, A&A, 669, A106
Eklund, H., Wedemeyer, S., Szydlarski, M., Jafarzadeh, S., & Guevara Gómez, J. C. 2020, A&A, 644, A152
Eklund, H., Wedemeyer, S., Snow, B., et al. 2021a, Phil. Trans. R. Soc. London, Ser. A, 379, 20200185
Eklund, H., Wedemeyer, S., Szydlarski, M., & Jafarzadeh, S. 2021b, A&A, 656, A68
Gudiksen, B. V., Carlsson, M., Hansteen, V. H., et al. 2011, A&A, 531, A154
Henriques, V. M. J., Jafarzadeh, S., Guevara Gómez, J. C., et al. 2022, A&A, 659, A31
Hofmann, R., Reardon, K., Milic, I., et al. 2022, ApJ, 933, 244
Högbom, J. A. 1974, A&AS, 15, 417
Iwai, K., Shimojo, M., Asayama, S., et al. 2017, Sol. Phys., 292, 22
Jafarzadeh, S., Rutten, R. J., Solanki, S. K., et al. 2017, ApJS, 229, 11
Jafarzadeh, S., Wedemeyer, S., Szydlarski, M., et al. 2019, A&A, 622, A150
Jafarzadeh, S., Wedemeyer, S., Fleck, B., et al. 2021, Phil. Trans. R. Soc. A: Math., 379, 20200174
Loukitcheva, M., Solanki, S. K., Carlsson, M., & Stein, R. F. 2004, A&A, 419, 747
Loukitcheva, M., Solanki, S. K., & White, S. 2006, A&A, 456, 713
Loukitcheva, M., Solanki, S. K., Carlsson, M., & White, S. M. 2015, A&A, 575, A15
Loukitcheva, M., White, S. M., Solanki, S. K., Fleishman, G. D., & Carlsson, M. 2017, A&A, 601, A43
Martínez-Sykora, J., De Pontieu, B., de la Cruz Rodriguez, J., & Chintzoglou, G. 2020, ApJ, 891, L8
McMullin, J. P., Waters, B., Schiebel, D., Young, W., & Golap, K. 2007, in Astronomical Data Analysis Software and Systems, eds. R. A. Shaw, F. Hill, & D. J. Bell (San Francisco, CA: ASP), ASP Conf. Ser., 376
Remijan, A., Biggs, A., Cortes, P., et al. 2020, ALMA Doc.8.3, ver. 1.0
Rodger, A. S., Labrosse, N., Wedemeyer, S., et al. 2019, ApJ, 875, 163
Shimojo, M., Bastian, T. S., Hales, A. S., et al. 2017, Sol. Phys., 292, 87
Szydlarski, M., Jafarzadeh, S., Eklund, H., & Wedemeyer, S. 2020, Solar ALMA Pipeline (SoAP) (1.0) https://doi.org/10.5281/zenodo.7351629
Vernazza, J. E., Avrett, E. H., & Loeser, R. 1981, ApJS, 45, 635
Wedemeyer-Böhm, S., Ludwig, H. G., Steffen, M., Leenaarts, J., & Freytag, B. 2007, A&A, 471, 977
Wedemeyer, S., Bastian, T., Brajša, R., et al. 2016, Space Sci. Rev., 200, 1
Wedemeyer, S., Szydlarski, M., Jafarzadeh, S., et al. 2020, A&A, 635, A71
White, S. M., Iwai, K., Phillips, N. M., et al. 2017, Sol. Phys., 292, 88
Wilson, T. L., Rohlfs, K., & Hüttemeister, S. 2013, Tools of Radio Astronomy (Berlin: Springer, Berlin Heidelberg)

Appendix A: Velocity distributions

The evolution of the vertical velocity at locations A and B of the two in-depth examples in the main text are given in Fig. A.1. The vertical velocity gives an indication of the up- and down-flow of the plasma at the different layers. The vertical velocity varies much in connection with the propagating shocks at location A, while it remains less dynamic and dominates the down-flow at location B in the network region.

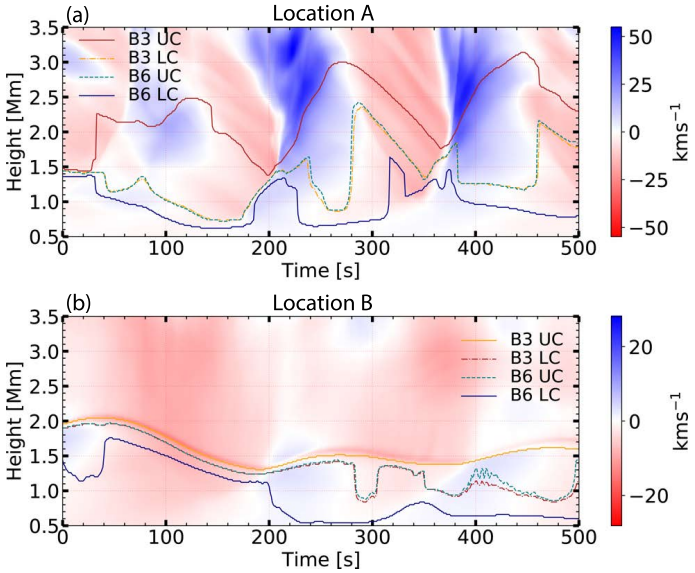

Fig. A.1. Time evolution of the vertical velocities of the columns at location A during the propagation of shock waves (a) and at location B in the network region (b). Upward motion, away from the photosphere, is indicated by negative velocity (blue). The representative formation heights of the lower and upper components of the observables for bands 3 and 6 are marked by the solid and dashed lines, respectively (see Sect. 3 in the main text for details).

Appendix B: Synthetic beam

The synthetic beams used to downgrade the brightness temperature maps are given in Table B.1. As the numerical Bifrost simulation does not represent a favoured orientation of the target on the Sun, all the setups were given the same position angle value of 80 degrees to enable more one-to-one comparisons of the resulting observables from the different antenna configurations.

Table B.1. Clean-beam parameters for SB3.1, SB3.4, SB6.1 and SB6.4 corresponding to that of ALMA array configurations $C1 - C7$ that were used for the simulated data. In the notation of the sub-band, they are preceded by the spectral band. The interferometric array configurations are those included in the simobserve tool in the Common Astronomy Software Applications package (CASA; v.6.1.0; McMullin et al. 2007) for observational cycle 5, C1 being the most compact and C7 more extended. We refer to Eklund et al. (2021b) for the statistics on the baseline lengths.
* The array configuration at this receiver band is currently not commissioned for solar ALMA observations.

Receiver band	Sub-band	ALMA Array configuration	Clean beam Major axis [arcsec]	Clean beam Minor axis [arcsec]	Clean beam Position angle [degrees]
Band 3	SB3.1	C1	4.46	3.90	80
	SB3.1	C2	3.28	2.83	80
	SB3.1	C3	2.12	1.78	80
	SB3.1	C4	1.33	1.18	80
	SB3.1	C5*	0.80	0.74	80
	SB3.1	C6*	0.51	0.40	80
	SB3.1	C7*	0.31	0.27	80
	SB3.4	C1	3.94	3.41	80
	SB3.4	C2	2.89	2.48	80
	SB3.4	C3	1.86	1.56	80
	SB3.4	C4	1.16	1.04	80
	SB3.4	C5*	0.70	0.65	80
	SB3.4	C6*	0.45	0.35	80
	SB3.4	C7*	0.27	0.23	80
Band 6	SB6.1	C1	1.86	1.63	80
	SB6.1	C2	1.38	1.17	80
	SB6.1	C3	0.89	0.75	80
	SB6.1	C4*	0.56	0.50	80
	SB6.1	C5*	0.34	0.30	80
	SB6.1	C6*	0.22	0.16	80
	SB6.1	C7*	0.18	0.10	80
	SB6.4	C1	1.73	1.52	80
	SB6.4	C2	1.29	1.09	80
	SB6.4	C3	0.83	0.70	80
	SB6.4	C4*	0.51	0.47	80
	SB6.4	C5*	0.31	0.28	80
	SB6.4	C6*	0.19	0.15	80
	SB6.4	C7*	0.17	0.10	80